PAPER

Highly nonlinear solitary waves for the detection of localized corrosion

To cite this article: Hoda Jalali and Piervincenzo Rizzo 2020 Smart Mater. Struct. 29 085051

View the article online for updates and enhancements.

You may also like

- Visualization of solitary waves via laser <u>Doppler vibrometry for heavy impurity</u> <u>identification in a granular chain</u> Feng Li, Liuxian Zhao, Zhenhua Tian et al.
- <u>Dynamics and spectral stability of soliton-like structures in fluid-filled membrane tubes</u>
 A. T. Il'ichev
- Optical solitary waves in thermal media with non-symmetric boundary conditions S A Louis, T R Marchant and N F Smyth





243rd ECS Meeting with SOFC-XVIII

Boston, MA • May 28 - June 2, 2023

Abstract Submission Extended Deadline: December 16

Learn more and submit!

Smart Mater. Struct. 29 (2020) 085051 (15pp)

Highly nonlinear solitary waves for the detection of localized corrosion

Hoda Jalali and Piervincenzo Rizzo

Laboratory for Nondestructive Evaluation and Structural Health Monitoring Studies, Department of Civil and Environmental Engineering, University of Pittsburgh, Pittsburgh, PA 15261, United States of America

E-mail: pir3@pitt.edu

Received 19 March 2020, revised 22 April 2020 Accepted for publication 10 June 2020 Published 21 July 2020



Abstract

This paper investigates the application of highly nonlinear solitary waves as a nondestructive evaluation method to detect localized corrosion in metallic structures. An experiment was conducted by using chains of monoperiodic particles in contact with a steel plate subjected to localized accelerated corrosion. A few damage-sensitive features were extracted from the time waveforms and fed into a multivariate statistical analysis to enhance the sensitivity of the proposed non-invasive monitoring approach. The experiment was complemented by a finite element model to quantify the effects of localized corrosion on certain features of the solitary waves propagating along the chain. Both the numerical and the experimental results show that the solitary waves reflected at the chain-plate interface are affected by the presence and progression of corrosion. Furthermore, the multivariate statistical analysis improved the sensitivity of the proposed approach. In the future, the proposed method may be implemented in those applications in which high temperature or radioactive environments are detrimental for the use of piezoelectric based ultrasonic testing.

Keywords: nondestructive evaluation, highly nonlinear solitary waves, outlier analysis, localized corrosion, finite element methods

(Some figures may appear in colour only in the online journal)

1. Introduction

Corrosion affects many engineering structures worldwide. For example, pipelines subjected to high temperatures in power plants and petrochemical industries are vulnerable to wall thinning corrosion and erosion-corrosion, which may lead to leakage and explosion. According to the U.S. PHMSA, in the last 20 years, nearly 6 000 incidents in pipelines have been reported in the U.S., causing more than 290 deaths and about \$10 billion in damage. Nearly 30% of these incidents were caused by corrosion [1]. Corrosion was also a significant contributing factor in about 20% of accidents in refineries in Europe [2]. Therefore, regular inspection and maintenance of pipelines are crucial to ensure safety and prevent adverse consequences for the economy and the environment.

Several nondestructive evaluation (NDE) methods exist for corrosion detection in pipes. The most important ones are ultrasonic testing [3–9], infrared thermography [10–12], and pulsed eddy current [13–17]. Although these methods have

been proved effective in detecting corrosion and wall thinning. They may be limited by the operating temperature of the pipelines, which force scheduled temporary shutdowns. For example, ultrasonic testing is not applicable at high temperatures because piezoelectric transducers, used to generate and detect the ultrasounds, are depolarized at temperatures higher than the Curie temperature (about 250 °C). Besides, the difference of the coefficient of thermal expansion at the interface between the transducer and the structure being inspected may cause noise or false positives. Therefore, there has been an increased interest in developing ultrasonic transducers that can be operated at high temperatures. These transducers use piezo materials like bismuth titanate and lithium niobite, which can operate up to 550 °C and 1 000 °C [18–22], respectively. However, the sensitivity of these piezo materials decreases over time [23]. Some researchers have proposed non-contact systems such as EMATs [24] and lasers [25, 26]. These solutions may have lower efficiency than conventional piezoelectric transducers or are too expensive to warrant widespread usage. A recent development was proposed by Cegla *et al* [23], who introduced a system in which thin waveguides separate the vulnerable piezo from the high-temperature area to be inspected [8, 23].

In the study presented in this paper, we propose an alternative NDE approach that can also be used for the 24/7 monitoring (structural health monitoring approach) of pipes and metallic structures, in general. The method relies on the propagation of highly nonlinear solitary waves (HNSWs) generated and propagating in an array of closely packed particles interacting via nonlinear contact forces under zero or weak precompression [27–37]. The overall principle of the proposed approach is schematized in figure 1. One end of an array of identical spheres is in dry contact with the structure to be inspected. An incident solitary wave (ISW) is generated at the opposite end of the chain and propagates along the array toward the surface of the structure. At the interface between the chain and the structure to be monitored, most of the acoustic energy carried by the ISW is reflected back, giving rise to one or two reflected solitary waves, typically referred to as the primary and the secondary reflected solitary waves (PSW and SSW). The main research hypothesis investigated in this study is that the characteristics of the reflected waves, and in particular of the PSW, are significantly affected by the amount of corrosion in the metallic structure being monitored.

Many researches showed that the amplitude and the arrival time of the reflected solitary waves depend on the mechanical and geometric properties of the adjacent structure/material [29, 37–48]. For example, Yang et al studied numerically, analytically, and experimentally the reflection of HSNWs at the interface between a chain of particles and a large thin plate, and found that the amplitude and the arrival time of the reflected waves are affected by the plate thickness, the particles size, and the boundary conditions at a critical distance from the plate boundaries [49]. Kim et al proved experimentally and numerically that solitary waves are effective at detecting delamination in a carbon fiber reinforced polymer composite plate [41]. A numerical study on the interaction of HNSWs with composite beams showed that solitary waves can be used to evaluate the directional elastic parameters of composites [50]. Others reported that the method is effective in detecting subsurface voids [48], and assessing the quality of adhesive joints [39, 40], composites [41, 44, 50, 51], orthopedic and dental implants [42, 52]. Other applications include but are not limited to the measurement of internal pressure in tennis balls [53–55] and the measurement of axial stress [56, 57].

As a term of comparison between the proposed method and conventional ultrasonic testing through-thickness measurements, the chain of particles represents the 'pulse-echo' transducer that acts as a transmitter of solitary waves and as a sensor for the same waves. If the particles are made of thermally insulating material, they act as a buffer between the structure and the sensing system embedded in the array. As such, a solitary wave-based NDE offers several advantages over classical NDE methods, including simplicity, low cost, and portability.

In order to establish the proposed HNSW-based method for detecting localized corrosion in metallic structures, it is essential to understand how these waves interact with pristine and corroded plates. Although there is a limited number of studies about the interaction of HNSWs with pristine plates, the interaction of HNSWs with damaged plates has not been investigated before. This paper aims to fill this gap of knowledge by presenting a numerical and an experimental study on a thin plate subjected to localized corrosion. The numerical analysis consisted of a coupled discrete/finite element model. The finite element model relied on the classical plate theory while the dynamic interaction between the granular chain and the plate was analyzed using the Hertz model. The experimental study consisted of monitoring localized corrosion in a steel plate with HNSW transducers. Ultrasonic testing was added to the experiment to compare corrosion monitoring results obtained from the HNSW-based method and conventional bulk ultrasonic testing. Both the numerical and experimental results demonstrate that HNSWs are affected by the propagation of localized corrosion in the plate. The results are discussed with respect to previous studies on the impact of spheres on plates [58–63]. To enhance the sensitivity of the method an outlier analysis (OA) was applied to the solitary wave data. OA is a novelty detection method that establishes whether a new configuration of the system being monitored is discordant or inconsistent from the baseline configuration, which consists of an existing set of data (or patterns) that describe the normal operative conditions. OA was applied in SHM for detecting structural damages in vibration analysis [64-68], ultrasonic guided waves [69-73], and HNSWs-based NDE [74].

This paper is organized as follows: section 2 describes the experimental setup. Section 3 presents the numerical model implemented here to study the application of HNSWs to detect localized corrosion in steel plates. The results obtained from the experimental and numerical studies are presented and discussed in section 4. Finally, section 5 ends the paper with some concluding remarks.

2. Experimental setup

The overall experimental setup is shown in figure 2. A 609.6 mm \times 609.6 mm \times 6.35 mm steel plate was half immersed in a 3.5% NaCl solution to induce accelerated corrosion through a conventional electrochemical corrosion process [3, 23, 75]. A copper sheet (electrode) was immersed in the solution and 10 V were applied between the steel and the copper plates using a DC power supply. The test specimen and the electrode were connected to the positive and the negative pole of the power supply, respectively. An oxygen diffuser was placed in the solution to increase the corrosion rate.

To induce localized corrosion, the wet face of the plate was covered in advance with corrosion resistant tape, and three square-shaped tape cores were removed with a cutter to expose the metal to the NaCl solution. The locations of these areas are labeled as A, B, and C in figure 2(b). One pulse-echo ultrasonic transducer (model Olympus DHC713) and two solitary wave transducers were placed on the dry side of the test specimen right above the areas A, B, and C, respectively, as summarized

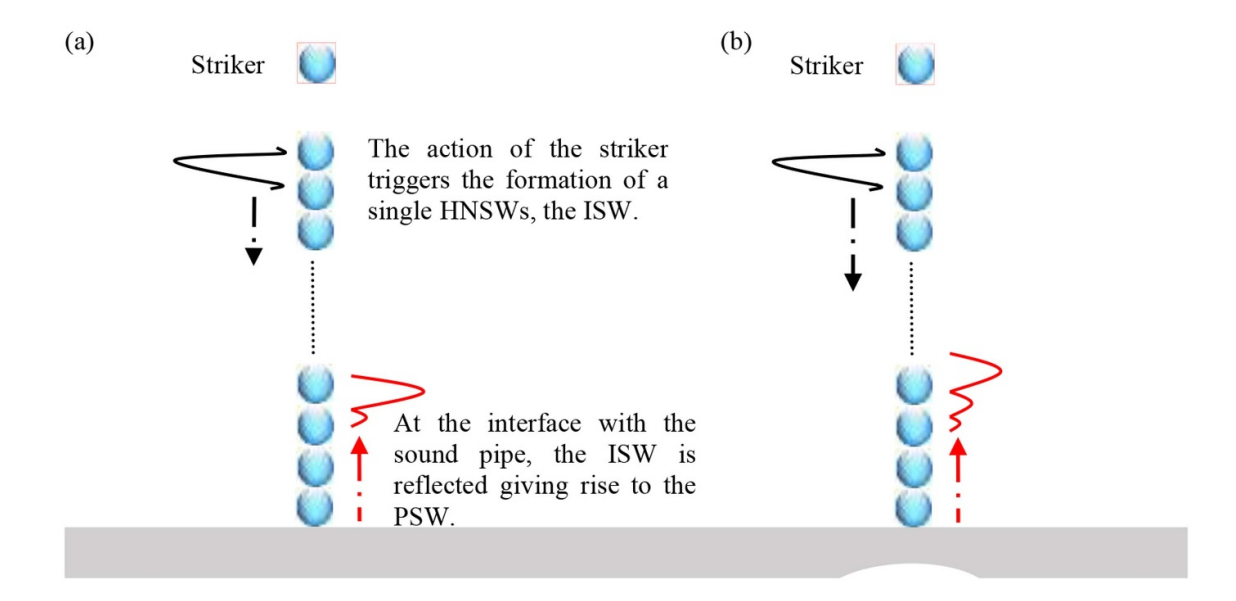


Figure 1. Scheme of the proposed NDE/SHM system. A chain of spheres is located above the metallic structure to be inspected. A solitary pulse (the incident solitary wave: ISW) is induced in the chain by the mechanical impact of the striker with the chain. The ISW reaches the surface of the metallic structure and is partially reflected back as the primary reflected solitary wave (PSW) to the chain. The research hypothesis investigated in this paper is that the shape, amplitude and time of flight of the PSW are monotonically dependent on the thickness of the metal

Table 1. Monitoring positions, methods, and the size of localized corrosion area under each transducer.

Monitoring Position	Monitoring Method	Corrsion Size (mm)			
A	Ultrasonic transducer	25.4 × 25.4			
В	HNSW transducer	25.4×25.4			
C	HNSW transducer	50.8×50.8			
D	HNSW transducer	Pristine			

in table 1. A third HNSW transducer was positioned on a part of the plate, protected by the tape. The position of this control HNSW transducer is labeled with the letter D in figure 2(b), and listed in table 1.

Each HNSW transducer (figure 2(c)) consisted of an array of eight 19.05 mm 28.2 gr spheres. All the particles except the top one (striker) were made of non-ferromagnetic stainlesssteel (type 440 C, elastic modulus E = 200 GPa and Poisson's ratio v = 0.28). Solitary waves were generated by lifting and releasing the ferromagnetic striker from a height of 5 mm. For this purpose, commercial electromagnets (Uxcell 12 V DC) were connected to and controlled by a National Instruments PXI running in LabVIEW. The repetition rate was set to 0.25 Hz, meaning that solitary pulses were generated every 4 s. The solitary wave force profiles were recorded by a sensor disk positioned in the middle of the chain between the fourth and the fifth particles. The sensor disk was made of a lead zirconate titanate (PZT) wafer, embedded between two 19.05 mm diameter, 6.05 mm thick disks. The PZT was insulated from the metal using Kapton tape.

The overall experimental setup is shown in figure 3. The specimen was monitored for about 350 h, and the areas subjected to localized corrosion were inspected on average

every hour. The monitoring intervals were shorter (30 min) during the initial portion of the experiment to provide a large baseline dataset for the statistical analysis. Each set of measurements included one ultrasonic signal recorded with the ultrasonic transducer and ten solitary wave signals taken with each HNSW transducer. The HNSW waveforms were sampled at 10 MHz while the ultrasonic signals were sampled at 100 MHz.

Around 270 h from the start, a through-thickness hole was detected at B, i.e. at the center of the plate (figure 4(a)). A close-up view of such defect is shown in figure 4(b). To prevent the free fall of the particles, the monitoring of this defect was terminated, but the experiment continued until a new through-thickness hole appeared close to location C (figure 4(c)). At the end of the experiment, the plate was removed from the tank and the protection tape was removed. Figure 4(d) presents the immersed face of the specimen: the presence of three pits is evident. For convenience, a close-up view of area C is shown in figure 4(e).

3. Numerical modeling

In the study presented in this paper, the dynamic interaction of HNSWs with a thin plate was numerically investigated using a discrete element (DE) model combined with a finite element (FE) analysis, all implemented in MATLAB[®]. The DE model simulates the propagation of HNSWs along the granular array, while the FE model describes the wave propagation in the plate. The two models were integrated at the contact point between the last particle of the array and the plate, as shown in figure 5(a).

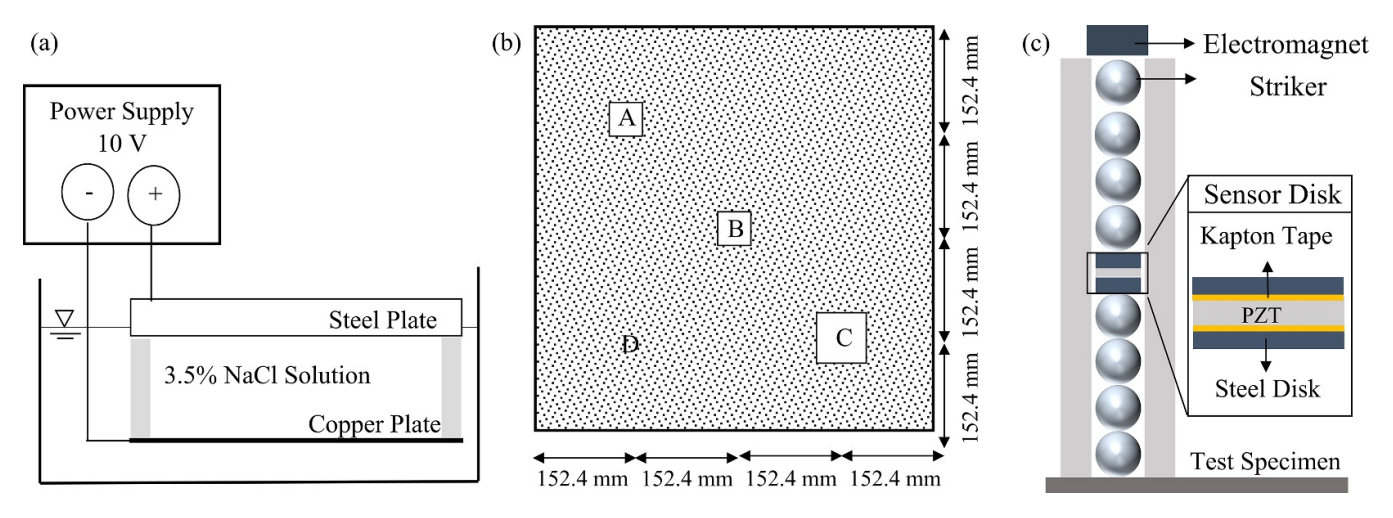


Figure 2. Experimental Setup. (a) Schematics of the accelerated corrosion test used to induce localized corrosion. (b) Dimensions of the steel plate and position of the areas subjected to localized corrosion. Area A is monitored with an ultrasonic transducer while areas B, C, and D are monitored with highly nonlinear solitary wave transducers. (c) Scheme of the HNSW transducer.

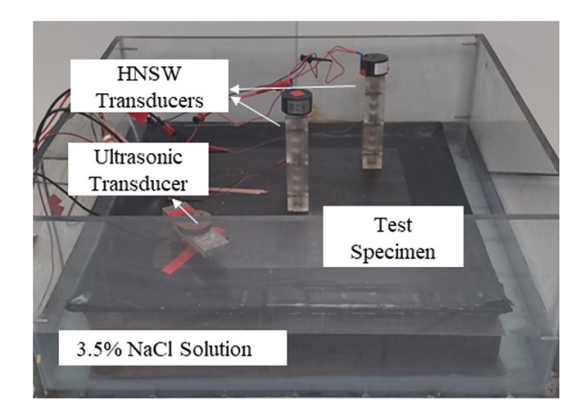


Figure 3. Photo of the overall experimental setup.

The DE model simulates the chain of particles as a series of point masses connected by nonlinear springs and dashpots (figure 5(b)). The interaction between two adjacent particles is modeled based on the Hertzian contact law as: $F = A\delta_+^{3/2}$. Here, the contact force F is proportional to the deformation δ of the diameter connecting the centers of the interacting beads through the stiffness coefficient A. The subscript + denotes the operator max $(\delta, 0)$ to indicate the absence of interaction force between two particles when they are separated from each other. For a chain of N identical spheres, the equation of motion of each particle is as follows:

$$\begin{split} m\ddot{u}_{i} &= A_{i-1,i} \left[u_{i-1} - u_{i} \right]_{+}^{3/2} - A_{i+1,i} \left[u_{i} - u_{i+1} \right]_{+}^{3/2} \\ &+ \gamma_{i-1,i} \left[\dot{u}_{i-1} - \dot{u}_{i} \right] \left[u_{i-1} - u_{i} \right]_{+} - \gamma_{i+1,i} \left[\dot{u}_{i} - \dot{u}_{i+1} \right] \\ &\left[u_{i} - u_{i+1} \right]_{+} + mg \end{split} \tag{1}$$

where m is the mass of the particle, g is the gravitational acceleration, and u_i and \dot{u}_i represent the displacement and the velocity of the i^{th} particle, respectively. As shown in figure 5(b), u_{N+1} represents the displacement of the plate at the contact point. The coefficient $A_{i,i+1}$ is the contact stiffness between

the i^{th} and the i + 1th particles:

$$A_{i,i+1} = \begin{cases} \frac{\frac{E_{b}\sqrt{2R}}{3(1-\nu_{b}^{2})} & i = 1:N-1, \\ \frac{4\sqrt{R}}{3} \left\lceil \frac{(1-\nu_{b}^{2})}{E_{b}} + \frac{(1-\nu_{p}^{2})}{E_{p}} \right\rceil & i = N. \end{cases}$$
 (2)

According to equation (2), the stiffness constant is a function particles radius R, the Poisson's ratio v, and the elastic modulus E of the particles and the plate. The subscript b indicates the properties associated with the beads, whereas the subscript p indicates the plate. Dissipation was introduced with the coefficient $\gamma_{i,i+1}$ (i=1:N-1) and set equal to 4.5 N.s.m⁻¹ in agreement with previous studies [38, 76]. The energy dissipation coefficient at the chain-plate interface ($\gamma_{i,i+1}$) was set to 34.05 N.s.m⁻¹ as reported in [38]. The FE and DE models were linked at the interaction point by sharing the relative nodal displacements.

The plate was meshed into 9216 elements (96 elements along each edge). As shown in figure 5(a), a finer mesh $(0.1 \text{ mm} \times 0.1 \text{ mm})$ was used near the interaction area between the plate and the granular chain to enhance the accuracy of the numerical results, whereas the element size along the edges increased with the distance from the plate-array interface in order to save computational time. The mesh refinement was determined based on a preliminary convergence test that showed that a further increase of the mesh density did not change significantly the properties of the solitary waves and the plate deformations. It is noted here that a similar refinement pattern was used in a numerical study on the detection of delamination in composite beams using HNSWs [41]. Figure 5(c) shows a 20 mm \times 20 mm element, located at the middle of the plate around the interface of the plate and the chain. The FE analysis was based on the Reissner-Mindlin plate theory in which the plate can be represented by its mid surface (figure 5(d)). Each element of the mesh (figure 5(e)) consisted of four nodes, and each node had three degrees of



Figure 4. Localized corrosion defects in the steel plate. (a) Top surface of the steel plate with a through-thickness hole detected in the corrosion area B. (b) A zoom in of the corrosion defect in the corrosion area B. (c) Through-thickness holes detected in the corrosion area C. (d) The corroded surface of the steel plate after removing the corrosion protection tapes. (e) A zoom-in view of the corrosion area C on the corroded surface of the steel plate.

freedom: transverse deflection w, rotation about the x-axis θ_x , and rotation about the y-axis θ_y .

With h representing plate thickness and ρ_p representing the density of the steel plate, the stiffness matrix \mathbf{k}_e of each element is given as [77]:

$$\mathbf{k}_{e} = \int_{A} \frac{h^{3}}{12} \left[\mathbf{B}^{I} \right]^{T} \mathbf{c} \mathbf{B}^{I} dA + \int_{A} \kappa h \left[\mathbf{B}^{O} \right]^{T} \mathbf{c}_{s} \mathbf{B}^{O} dA.$$
 (3)

The first and second terms in equation (3) represent the bending and shear stiffness, respectively. The strain matrices ${\bf B^I}$ and ${\bf B^O}$ depends on the element shape functions and their derivatives [77]. The parameter κ represents the shear correction factor for rectangular cross-sections equal to 5/6. The material matrix ${\bf c}$ is given by:

$$\mathbf{c} = \frac{E_{\rm p}}{1 - \nu_{\rm p}^2} \begin{bmatrix} 1 & \nu_{\rm p} & 0 \\ \nu_{\rm p} & 1 & 0 \\ 0 & 0 & (1 - \nu_{\rm p})/2 \end{bmatrix}. \tag{4}$$

Also, the material matrix $\mathbf{c_s}$ is defined as:

$$\mathbf{c}_{s} = \frac{E_{p}}{1 + v_{p}} \begin{bmatrix} 1 & 0 \\ 0 & 1 \end{bmatrix}. \tag{5}$$

In this study, the plate element stiffness matrix, \mathbf{k}_e , was calculated by integrating equation (3) numerically using 5×5 Gauss points of integrations. Similarly, the element mass matrix, \mathbf{m}_e , was calculated by numerical integration:

$$\mathbf{m}_{e} = \int_{A} \mathbf{N}^{T} \mathbf{I} \mathbf{N} dA, \qquad (6)$$

where N represents the shape function matrix as presented in [77], and I is given by:

$$\mathbf{I} = \begin{bmatrix} \rho_{\rm p}h & 0 & 0\\ 0 & \rho_{\rm p}h^3/12 & 0\\ 0 & 0 & \rho_{\rm p}h^3/12 \end{bmatrix}. \tag{7}$$

In the numerical simulation, the plate was simply supported along the four edges, and the elastic properties of the steel plate and the steel particles were as E=200 GPa, $\nu=0.3$, and $\rho=7~800$ kg.m⁻³. The localized corrosion

defect was modeled at the midpoint of the plate by reducing the thickness h of the plate elements from the baseline value of 6.35 mm. The dynamic response of the system was calculated by solving the nonlinear equations of motion in MATLAB using the solver ode45. The solitary wave profile at the sensor particle was obtained by averaging the interaction forces between the sensor particle and its adjacent particles [32, 50].

To validate the accuracy of the aforementioned model, a second modeling approach was implemented. A coupled DE/FE was modeled in ABAQUS/Standard as discussed in [50]. Figure 6(a) presents the scheme of the model. Due to the two symmetry planes in the problem, only one quarter of the geometry was modeled. The propagation of the solitary waves in the chain was simulated using a DE model. The chain of particles was modeled as eight mass points of mass m/4, interacting with nonlinear axial connectors. The nonlinear connectors were defined such to resemble the Hertzian contact law and the damping in the chain as depicted in figure 5(b). The nonlinear stiffness of the connectors was equal to $A_{i,i+1}/4$ for i = 1:N-1 in equation (1) since only one quarter of the geometry was modeled.

The last particle in the chain and the plate were modeled as deformable solid parts, and their geometric and mechanical properties were identical to those used in the previous model. The plate was simply supported along two edges, and the symmetry boundary conditions were applied on all the nodes on the two planes of symmetry. Moreover, boundary conditions were imposed on the point masses (m1 to m8) so that they could move only along the chain axis. The contact between the last particle and the plate was modeled using the hard contact interaction with frictionless tangential behavior. Both the plate and the particles were meshed using 3D 8-node linear isoparametric elements (C3D8 in ABAQUS). As shown in figure 6(b), the mesh size gradually decreases to 0.5 mm near the interface of the particle and the plate to improve the accuracy of deformations and stresses calculated at the interface.

The DE and the FE models were coupled by connecting the last point mass in the DE model (m8) to the uppermost node of the 3D particle using the nonlinear connectors described earlier. To generate solitary waves in the model, an impact velocity of $V_{imp} = 0.31 \text{ m.s}^{-1}$ was applied to the

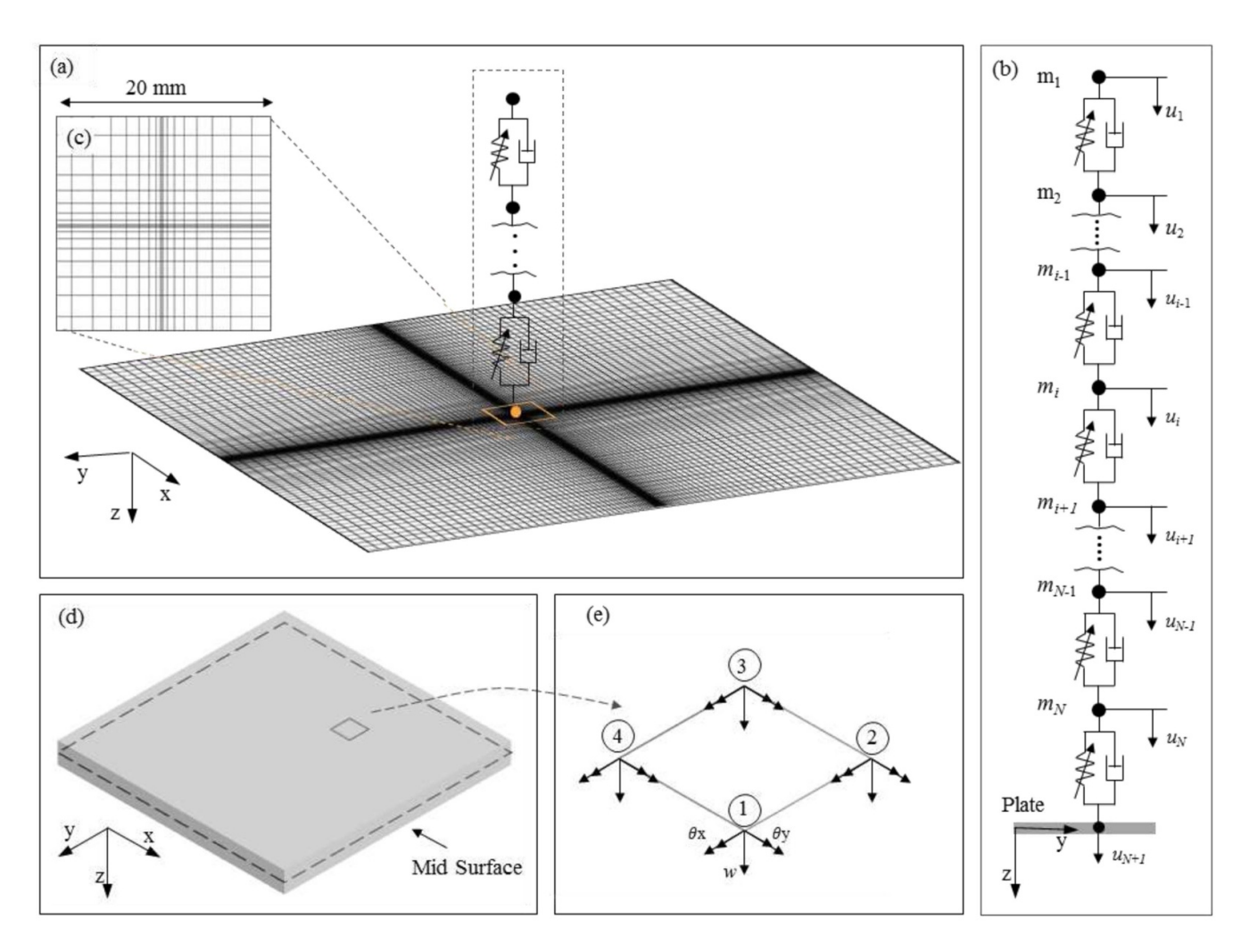


Figure 5. Numerical model of the interaction between the granular chain and the plate. (a) The coupled discrete element (DE) and finite element (FE) models integrated at the contact point between the array of particles and the plate. (b) Schematic of the DE model. (c) A zoom-in of the mesh refinement pattern in a square of $20 \text{ mm} \times 20 \text{ mm}$ in the middle of the plate. (d) The mid surface representing the plate in the FE model and (e) the nodes and the degrees of freedom of each plate element.

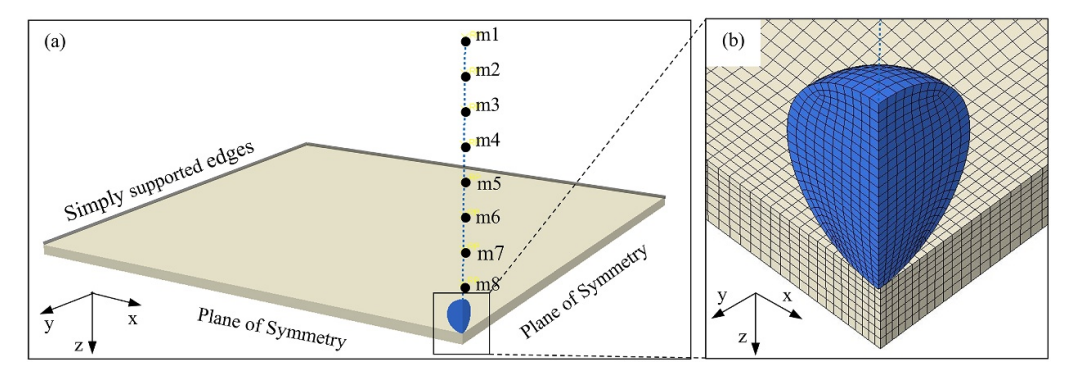


Figure 6. ABAQUS model of the interaction between the granular chain and the plate. (a) The coupled coupled discrete element (DE) and finite element (FE) models. One quarter of the model is stimulated due to symmetry. (b) Zoom-in view of the FE model meshing at the interface between the chain and the plate.

first mass point in the chain (m1). The effect of gravity was also considered by applying proper body forces to the plate and the 3D particle. Also, concentrated forces of w = mg/4 were applied on each point mass in the chain. The nonlinear equations of equilibrium were solved in ABAQUS/CAE,

and the particles displacement were extracted from the numerical results. The solitary wave profiles at the sensor particle were then calculated by averaging the interaction force between this particle and its upper and lower adjacent particles.

4. Results and discussion

Figure 7 displays the experimental solitary waves recorded by the HNSW transducers positioned above the areas B, C, and D. Each waveform is the average of the ten measurements taken at a given instant. The first pulse around 150 μ s is the ISW traveling towards the chain-plate interface. The amplitude of this pulse is expected to remain constant regardless of the conditions of the plate. The subsequent pulses represent the PSW and SSW, respectively. For clarity, the arrival of the SSWs is boxed in red rectangles. Figures 7(a) and (b) are relative to the corroded areas B and C, respectively. They show a shift in the time of arrival and a decrease in amplitude of the PSW after measurement 150, i.e. about 75 h within the experiment. For convenience, these sets are emphasized with the red circles.

The time of flight (ToF) of the PSW was calculated as the difference between the ISW and the PSW peaks. The results are presented in figure 8. The graphs relative to the corroded area (figures 8(a) and (b)) show a moderate increase of the feature with the progression of corrosion. On the other hand, figure 8(c) shows that the ToF measured above the pristine area D remains relatively constant throughout the experiment. While the ToF associated with the pristine area was about $325 \mu s$, the same feature measured under extensive corrosion increased by about 10% (figures 8(a) and (b)).

To quantify a trend between ToF and the time, a 2nd order polynomial regression was fitted to the experimental data (dashed lines in figure 8). The 2nd order was used since the numerical results (discussed later in the paper) show a nonlinear trend of the ToF with respect to the progression of the corrosion. The coefficients of the regressions are similar for the two transducers placed above the corroding areas (figures 8(a) and (b)). Moreover, all regressions display that ToF at the beginning of the experiment (Time = 0 hr.) was about 325 μ s. This indicates little if no variation in the fabrication and assembly of the solitary wave transducers.

Leveraging upon previous studies from the authors' group, the normalized amplitude of the PSW with respect to the amplitude of the ISW (also referred to as amplitude ratio) was computed, and the results are presented in figure 9. The graphs show a 30% decrease of this solitary wave feature as localized corrosion propagates in areas B and C. As the normalized amplitude relative to area D remained mostly constant (figure 9(c)), it can be concluded that this feature is significantly affected by the presence of localized corrosion. By looking at the coefficient of the 2nd order polynomial, it can be said that under pristine conditions at Time = 0 hr, about half of the incident acoustic energy is reflected back as a PSW and this is consistent for all three transducers. Also, the regression coefficients are nearly the same for the two transducers above the corroding areas. The difference in the x² coefficient is because corrosion propagated faster at area B, resulting in a through-thickness hole in the plate after 270 h.

To interpret the experimental findings, the effects of localized corrosion on the solitary wave features are approximated with the analytical Zener model [58], which describes the impact of one sphere on a large thin uniform plate. This model assumes that the impact is not perfectly elastic and part of the kinetic energy of the impact is dispersed by the propagation of flexural elastic waves in the plate [49, 58–60]. A coefficient of restitution e, comprised between 0 and 1, is introduced and defined as the ratio of the reflected to the incident velocity. Zener [58] described the impact by coupling the equations of motion of the plate and the sphere, leading to the following nonlinear equation in term of the dimensionless time (τ) and dimensionless approach (σ) [49, 58–60]:

$$\frac{\mathrm{d}^2\sigma}{\mathrm{d}\tau^2} + \left(1 + \lambda \frac{\mathrm{d}}{\mathrm{d}\tau}\right)\sigma^{\frac{3}{2}} = 0,$$

$$\begin{cases}
\sigma = 0 \\
d\sigma/d\tau = 1
\end{cases} \text{ at } \tau = 0, \tag{8}$$

where the inelasticity parameter, λ , is defined as:

$$\lambda = \frac{\pi^{3/5}}{4\sqrt{3}} \left(\frac{2R}{h}\right)^2 \left(\frac{\rho_{\rm b}}{\rho_{\rm p}}\right)^{3/5} \left[\frac{v_{\rm in}^2 \rho_{\rm p} \left(1 - v_{\rm p}^2\right)}{E_{\rm p}}\right]^{1/10}$$

$$\left[1 + \frac{E_{\rm p} \left(1 - v_{\rm b}^2\right)}{E_{\rm b} \left(1 - v_{\rm p}^2\right)}\right]^{-2/5}.$$
(9)

Here, v_{in} denotes the incident velocity of the sphere while the other parameters were introduced in section 3. The coefficient of restitution e can be calculated by solving equation (8) for a given λ . Figure 10(a) presents the coefficient e as a function of λ calculated numerically by Zener [58] and more recently by analytical approximations [60]. The solid line shows the numerical solution, and the dashed line presents an analytical approximation equation proposed for $\lambda < 1$ [60]:

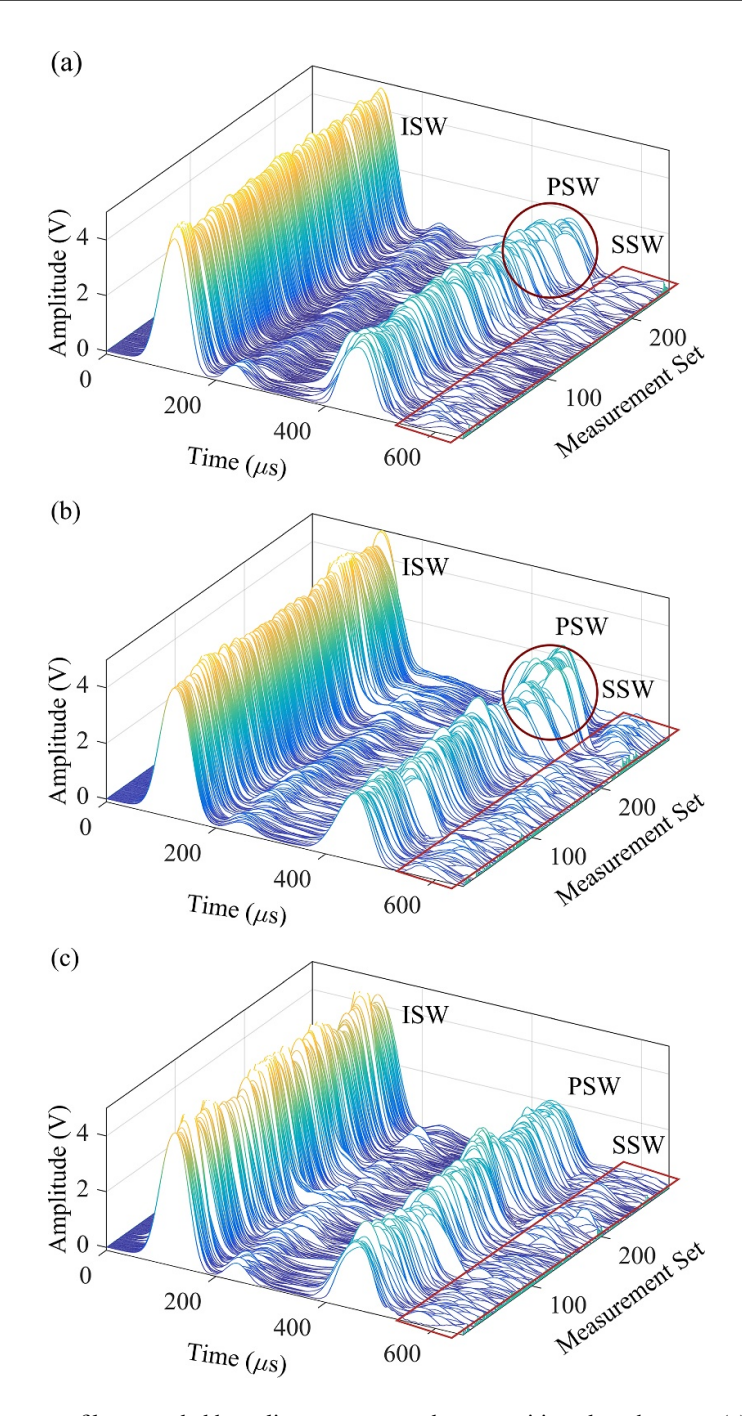
$$e \approx \exp\left(-1.6605\lambda\right). \tag{10}$$

Based on equation (9), as the plate thickness h decreases, the parameter λ increases. Furthermore, figure 10(a) shows that the coefficient of restitution decreases as the inelasticity parameter increases. Therefore, thickness reduction results in a lower coefficient of restitution because more energy is dissipated during the impact.

A unique characteristic of HNSWs is that their velocity V is proportional to $F_{\rm m}^{1/6}$, where $F_{\rm m}$ is the maximum dynamic force between particles [27, 78]. It implies that stronger pulses propagate faster. In addition, the velocity V is proportional to $v_{\rm m}^{5/6}$, where $v_{\rm m}$ is the maximum particle velocity. Therefore, the normalized amplitude of the PSW (AR) discussed in figure 9 can be expressed in terms of the coefficient of restitution [49, 74] as:

$$AR = \frac{F_{\text{m,PSW}}}{F_{\text{m,ISW}}} = \left(\frac{V_{\text{PSW}}}{V_{\text{ISW}}}\right)^6 = \left(\frac{v_{\text{m,PSW}}}{v_{\text{m,ISW}}}\right)^{6/5} = e^{6/5}.$$
 (11)

Based on the discussion in the previous paragraph and equation (11), it can be concluded that the normalized amplitude is expected to decrease as the thickness of the plate



 $\textbf{Figure 7.} \ \ \text{Solitary wave profiles recorded by solitary wave transducers positioned on the areas (a) B, (b) C, and (c) D. \\$

decreases, as confirmed experimentally and numerically elsewhere [49, 62, 63].

The aforementioned studies delved with plates of uniform thickness. However, the concept of inelasticity parameter can be adopted at large in this study to explain the effect of localized corrosion on the solitary wave features. Under such approximation, it can be argued that localized corrosion increases the value of λ locally with yielding to a local decrease in the coefficient of restitution and normalized amplitude.

Figure 10(b) shows the dimensionless contact time τ_c as a function of λ . It is noted here that the numerical solution (he

continuous line in the graph) was obtained by Zener [58] solving equation (8) and plotted here using data points presented in [58]. The analytical approximation is instead based on the equation proposed by Muller *et al* [63]:

$$\tau_{\rm c} = 2.762 + 0.4568 \exp(1.27\lambda)$$
. (12)

In an uncompressed chain of particles, ToF can be approximated as [49]:

$$TF = \left[1.18\left(1 + e^{-1/5}\right)NA|_{s}^{-2/5} + 1.08\tau_{c}A|_{p}^{-2/5}\right]m^{2/5}v_{imp}^{-1/5},$$
(13)

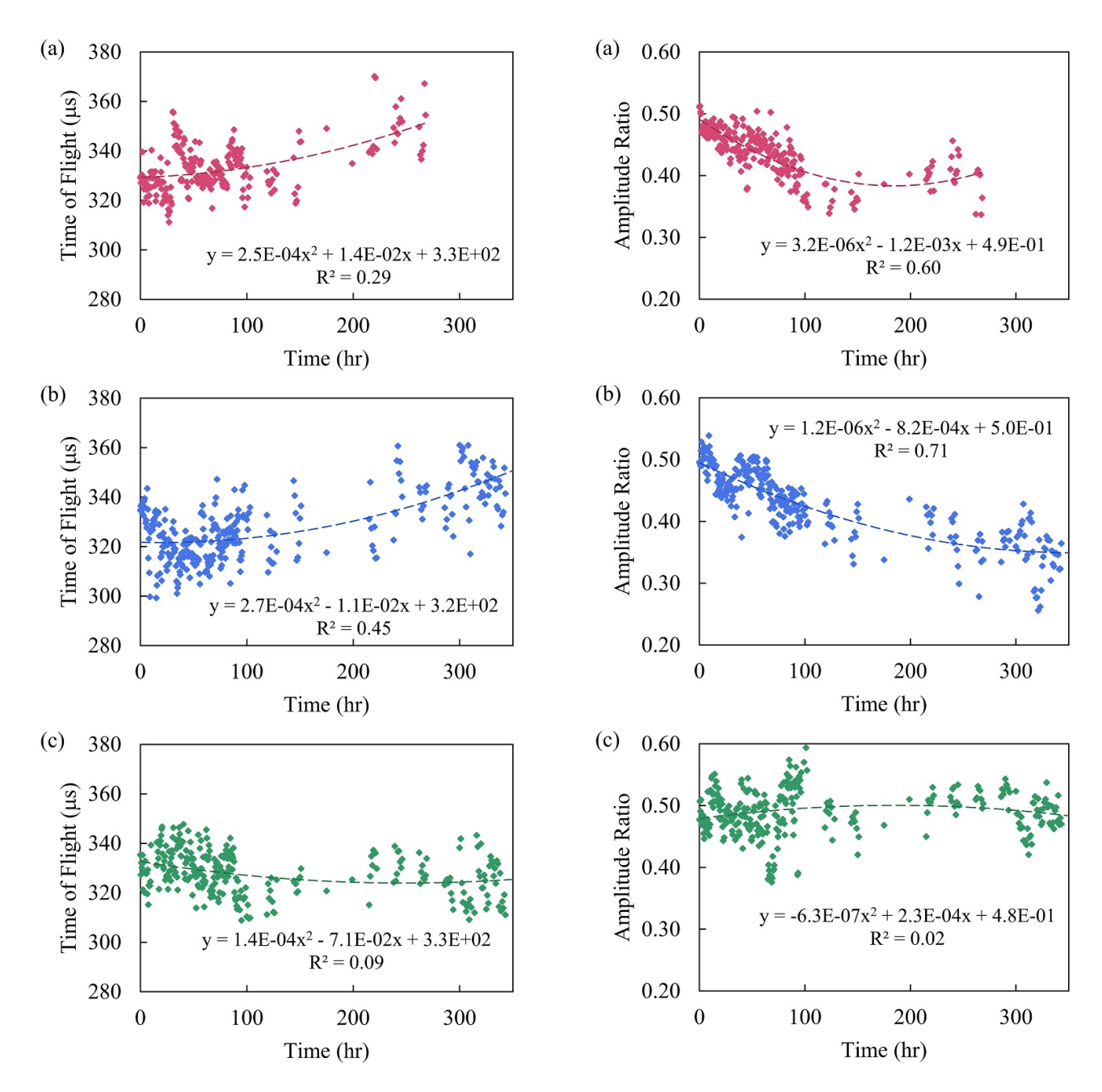
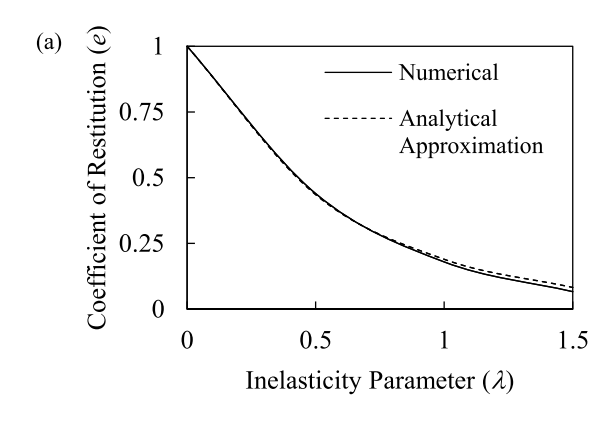


Figure 8. Experimental results. Time of flight, calculated by the peak to peak method for solitary wave transducers used to monitor areas (a) B, (b) C, and (c) D of the test object.

Figure 9. Experimental results. Normalized amplitude of the primary reflected solitary wave measured from the areas (a) B, (b) C, and (c) D monitored with the HNSW transducer.

where N is the number of particles between the sensor and the structure being inspected, in the present study the metallic plate. Here, N is equal to 4. The coefficients $A|_{\rm s}$ and $A|_{\rm p}$ are the stiffness constants defined in equation (2), corresponding to cases of i=1: N-1 and i=N, respectively. Also, the parameters m and $v_{\rm imp}$ represent the mass of the spheres and the speed of the striker at the impact, respectively. According to equations (12) and (13), as the inelasticity parameter increases, the dimensionless contact time $\tau_{\rm c}$ and the TF increase. Thus, localized corrosion is expected to increase the ToF, as observed in figures 8(a) and (b).

To verify that the trends observed in figures 8 and 9 are not biased by any variation of the amplitude of the ISW, which in turn it may be affected by the collision of the striker with the chain, figure 11 is presented. It shows the amplitude of the ISW as a function of time, for all the three transducers. Each dot represents the average of the ten measurements. The graphs show no trend for the three transducers, and the regression suggests that the fabrication and assembly of the transducers were consistent. The random variability of the ISW amplitude can be therefore attributed to the inherent stochastic nature of the striker collision [79] and occasional tilting of the sensor disk.



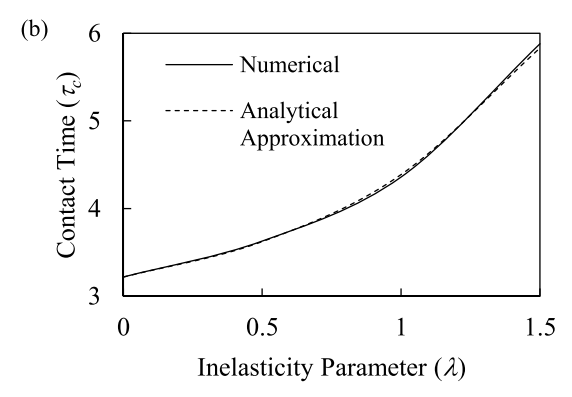


Figure 10. (a) Coefficient of restitution (e) and (b) contact time (τ_c) as a function the inelasticity parameter (λ) .

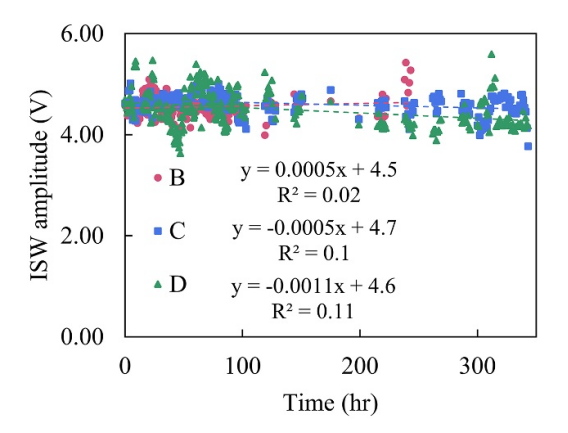


Figure 11. Experimental results. Amplitude of the incident solitary wave.

To investigate further and quantify the effect of the ISW amplitude on the ToF and normalized amplitude of the PSW, the analytical Zener model and our numerical model was applied for two case scenarios in which the amplitude of the ISW is increased and decreased by 20%. The pristine plate described in section 3 and shown in figure 5 was considered. The results are presented in figure 12 and show that the \pm 20% change in the ISW amplitude yields to \pm 2.5% in ToF and \pm 1.5% in amplitude ratio. Figure 12 also presents such effect using the analytical Zener model in dashed lines. Table 2 summarizes the calculations of *ToF* and amplitude ratio AR in the analytical model for cases of different striker falling heights (h_s) . The striker velocities (v_{imp}) calculated as $\sqrt{2gh_s}$ is presented in the third column, and the maximum velocity of the particles in the chain ($v_{\rm m} \approx 0.682v_{\rm imp}$ [80]) is presented in the fourth column. The normalized ISW amplitude with respect to case #3 (the case of $h_{\rm s}=5$ mm) was calculated using $F_i/F_3 = (v_{m,i}/v_{m,3})^{6/5}$. The equations used to calculate other parameters are specified on the same

According to figure 12, both the numerical and analytical results show that the amplitude of the ISW has little effect on the wave features associated with the primary reflected wave when compared to the 10% and 30% change observed empirically in figures 8 and 9. Therefore, figures 12 confirms

that the variations observed in figures 8 and 9 were truly related to the localized corrosion.

According to figure 12, the ToF predicted with the numerical model is very close to the experimental value, 319 μ sec vs 325 μ sec measured for the pristine plate and shown in figure 8. The large offset with the ToF predicted with the analytical model (calculated by equation (13)) is likely attributable to the fact that this model does not consider the precompression due to gravity and the energy dissipation in the granular chain. Due to the tunability properties of solitary waves, adding precompression to the granular chain increases the solitary wave propagation speed and decreases ToF. In addition, the analytical model describes the impact of spheres directly onto thin plates, while the thin plate assumption may not hold valid for the 6.35 mm thick plate tested in this study.

Conversely, the amplitude ratio predicted numerically and shown in figure 12(b) overestimates the experimental values shown in figure 9, i.e. 0.837 vs 0.500. This difference is likely attributable to the absence of dissipative effects in the model and to an underestimation of the dissipation coefficient γ . To verify this latter hypothesis, figure 12 shows the two wave features relative to a 'modified numerical model' in which the dissipation coefficient at the chain-plate interface ($\gamma_{N,N+1}$) was set equal to 1 000 N.s.m⁻¹ (refer to equation (1)). The results show that the coefficient γ at the array-structure interface affects significantly the amplitude ratios whereas it has minor effects on the ToFs.

To better interpret the experimental data and generalize the NDE protocol, two finite element models were developed as discussed in section 3. Figure 13 presents the numerical results for the interaction of HNSWs with the steel plate considered in the experiment and containing a corrosion-like defect of size 25.4 mm \times 25.4 mm at the plate center. The corrosion depth varies from 0 (pristine plate) to 80% of the thickness. According to figure 13(a), the MATLAB model suggests the increase of TOF from 319 μ s to 355 μ s as the corrosion propagates, which is in excellent agreement with the experimental results presented in figures 8(a), (b), 15(a) and (b). The ABAQUS model results also suggest an increase in ToF from 326 μ s to 379 μ s as the corrosion propagates. Both the models show a nonlinear trend in ToF as a function of corrosion depth.

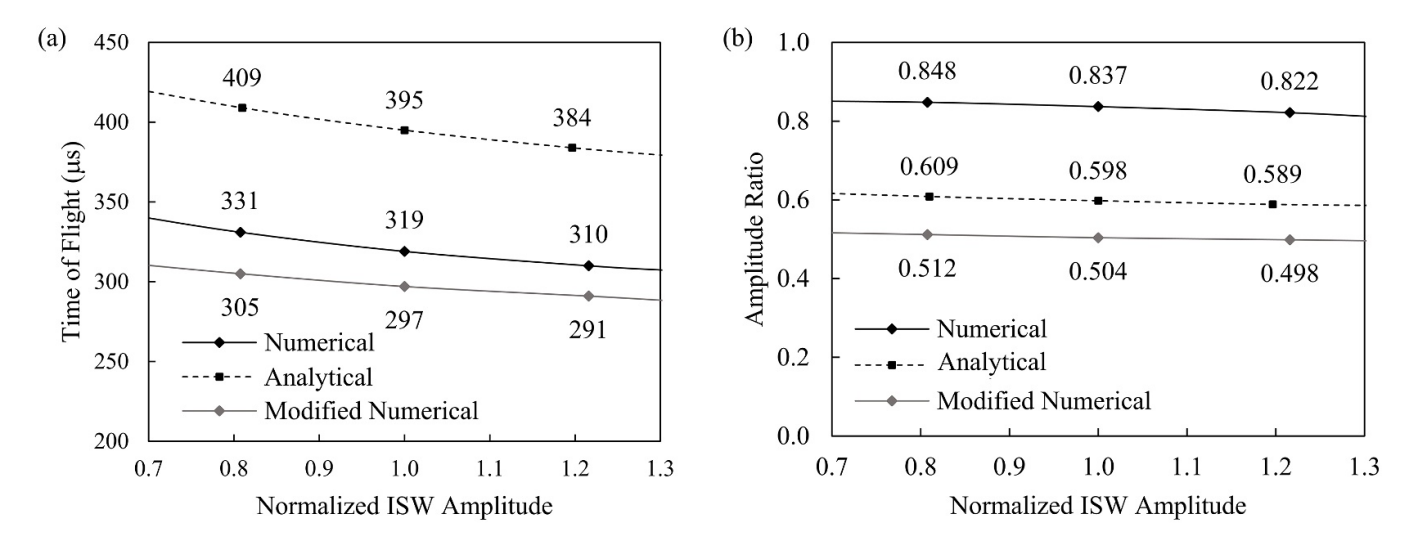


Figure 12. The effect of the incident solitary wave amplitude on the solitary wave features: (a) time of flight, and (b) amplitude ratio.

Table 2. Effect of ISW on ToF and amplitude ratio based on the analytical Zener Model.

Case #	h _s (mm)	v _{imp} (m/s)	<i>v</i> _m (m/s)	AR w.r.t. case 3	λ (equation (9))	e (equation (10))	AR (equation (11))	$ au_{\rm c}$ (equation (12))	TOF (μ s) (equation (13))
1	2.0	0.20	0.14	0.59	0.237	0.68	0.624	3.38	430
2	3.5	0.26	0.18	0.81	0.249	0.66	0.609	3.39	409
3	5.0	0.31	0.21	1.00	0.258	0.65	0.598	3.40	395
4	6.5	0.36	0.25	1.20	0.266	0.64	0.589	3.40	384
5	8.0	0.40	0.27	1.36	0.273	0.64	0.585	3.41	377

Legend. h_s : striker Falling height; v_{imp} : striker velocity; v_m : maximum particle velocity; AR: normalized ISW Amplitude; λ : inelasticity parameter; e: coefficient of restitution; τ_c : dimensionless Contact Time; TOF: time of flight.

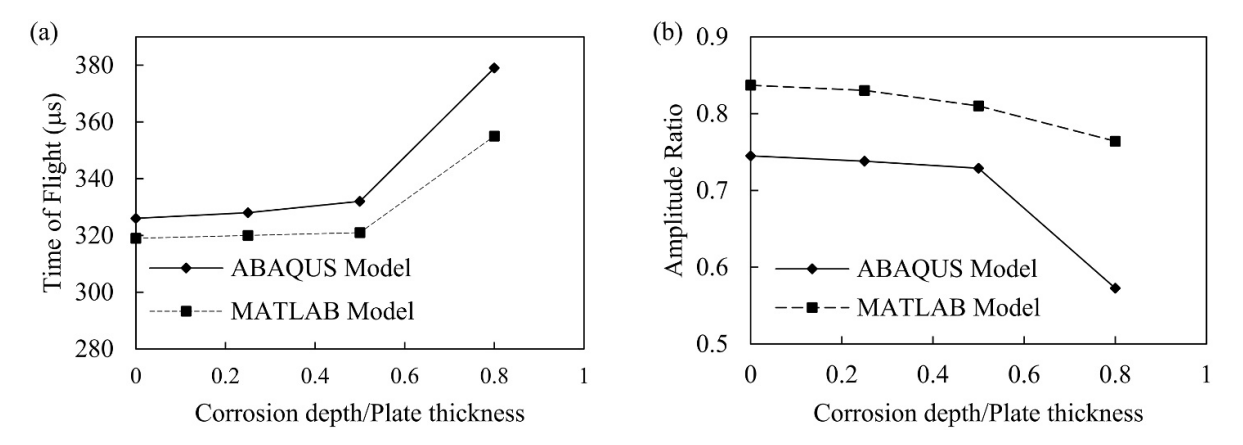
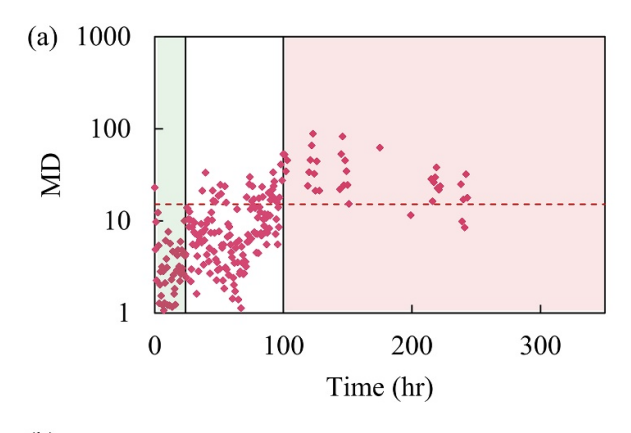


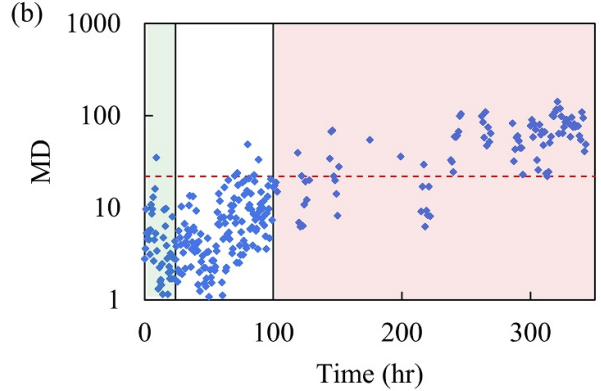
Figure 13. Numerical results. (a) Time of flight as a function of relative corrosion depth. (b) Amplitude ratio as a function of relative corrosion depth.

In fact, the numerical results suggest that the sensitivity of ToF to localized corrosion increases as the relative depth of localized corrosion is higher than 0.5.

In addition, figure 13(b) shows that the amplitude ratio decreases from 0.74 to 0.57 (ABAQUS model) and 0.84 to 0.76 (MATLAB model) as the relative corrosion depth increases. As presented in figures 9(a) and 8(b), the experimental results show an amplitude ratio changing from around 0.49 to around 0.35 as the localized corrosion penetrates in the

plate. As shown in figure 12(b) the amplitude ratio of the MAT-LAB model can be fitted to the experimental results by modifying the dissipation coefficient. The amplitude ratios obtained from the ABAQUS model is closer to the experimental data, since the 3D modeling of the impact between the last particle and the plate, allows capturing energy dissipation during the impact. The overestimation of the amplitude ratio in ABAQUS could show underestimating the energy dissipation in the chain in the ABAQUS model.





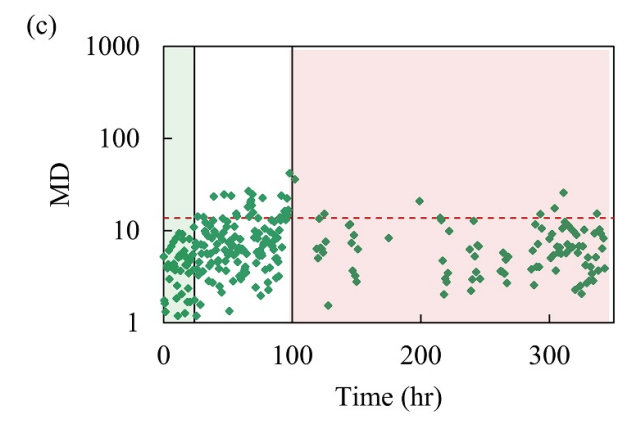


Figure 14. Multivariate outlier analysis. Mahalanobis distance calculated based on the five solitary wave features including time of flights calculated by the peak to peak method and the correlation method, amplitude ratio, autocorrelation coefficient, and area under the primary reflected solitary wave in areas (a) B, (b) C, and (c) D. The horizontal lines represent the 99.7% confidence threshold calculated as 19.7, 17,1, and 14,4, respectively. The green background presents the baseline data.

To explore additional wave features that may enhance the sensitivity of the proposed approach, the area under the PSW and the auto-correlation technique were also considered. The former quantifies the restituted acoustic energy at the chain-plate interface while the correlation provides another mean to calculate the travel time. Although the correlation method has been widely used to extract ToF in other NDE techniques like ultrasonics [81–83], it has not been reported in the literature for the analysis of solitary waves. Overall, the trends

of the correlation and the PSW area with respect to the progression of corrosion were similar to what observed in figures 8 and 9 and are not shown here for the sake of space.

The solitary wave features were clustered to perform an OA based on the Mahalanobis squared distance (MSD). The OA is an unsupervised learning algorithm based on novelty detection. It establishes whether a new configuration of the system is discordant or inconsistent from the baseline configuration which consists of an existing set of data (or patterns) that describes the normal operative conditions. Ideally, if the OA is used for detecting damaged states, the baseline should include normal variations in environmental or operative conditions of the structure (e.g. temperature, humidity, loads). However, it is generally difficult to account for all of the environmental variables that may affect a damage-sensitive set of features. The MSD is a multivariate data analysis in which several parameters, ideally all sensitive to the presence of damage, are considered. In this study, five parameters were considered: the ToF calculated with the peak to peak method and the correlation method, the normalized amplitude of the PSW, the autocorrelation coefficient, and the area under PSW. The MSD for each measurement set D_{ζ} was calculated as:

$$D_{\zeta} = (\{x_{\zeta}\} - \{\bar{x}\})^{T} [K]^{-1} (\{x_{\zeta}\} - \{\bar{x}\}), \qquad (16)$$

where $\{x_\zeta\}$ represents the potential outlier vector, $\{\bar{x}\}$ is the mean vector of the baseline, and [K] is the covariance matrix of the baseline. For each transducer, the baseline consisted of the measurements taken during the first 24 h of the experiment. The calculated MSD values are presented in figures 14 and the baseline data is highlighted in the green background. The threshold corresponding to the 99.73% confidence interval is shown by the horizontal dashed lines. The threshold values were calculated as the upper value of 3σ of the baseline and is equal to 21.9, 15.4, and 13.7 in figures 14(a)–(c), respectively. A value of the distance higher than the threshold represents an outlier, implying anomalies in the recorded data with respect to the database.

The effectiveness of the outlier analysis in detecting localized corrosion is evaluated based on the HNSWs features recorded after 100 h (highlighted in the red background on figure 14). According to figures 14(a) and 14b, 80% and 92% of the points in the red box show outliers in the recorded data of the corroding areas B and C, respectively. Sensitivity improves to 100% after 230 h, as the localized corrosion progress in area C (figure 14(b)). On the other hand, MSD calculated using the data recorded at the pristine area D (presented in figure 14(c)) shows only 8% outliers after 100 h (false positives). As shown in figure 14(c), those points are slightly higher than the threshold line, and they present false positives in the test. It can be concluded that using the multivariate outlier analysis is effective in detecting anomalies in the HNSW-based corrosion detection.

To compare the sensitivity of the proposed method with the sensitivity of the ultrasonic-based testing, figure 15 shows the ultrasonic time of flight measured by the pulse-echo transducer located above the corroded area A. The corresponding plate

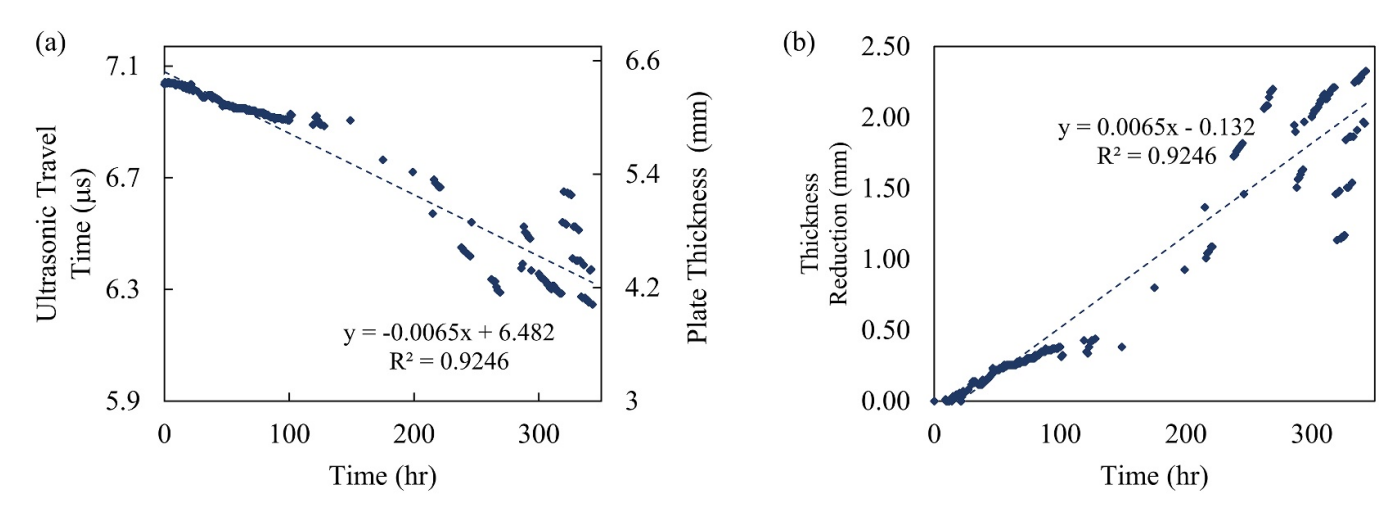


Figure 15. Ultrasonic test results. (a) Ultrasonic travel time in the corrosion area A (on the left axis) and the relative local plate thickness (on the right axis). (b) Plate thickness Reduction in area A obtained from the ultrasonic test results.

thickness reduction (Δth) and the remaining plate thickness (th) was estimated as:

$$\Delta th = \frac{UT_0 - UT}{UT_0 - D}th_0,$$

$$th = th_0 - \Delta th, \tag{17}$$

where th_0 denotes the initial plate thickness equal to 6.35 mm, UT_0 and UT denote the initial and the current ultrasonic travel time obtained from the correlation method, and D represents the dual transducer delay. The estimated values of the remaining plate thickness and the plate thickness reduction in the area A are shown in figure 15(a) (on the left axis) and figure 15(b), respectively. The graphs show an overall linear trend of the corrosion with respect to the time of the experiment. According to the estimate from the ultrasonic transducer, after 300 h the plate under probe was about 4.2 mm, i.e. about 36% thinner. At the end of the experiments, this area A was cored to forensically quantify the true thickness. It was found that the corrosion was not uniform and the real thickness varied between 2 mm and 5 mm. At the point where the ultrasonic transducer was located, the measured thickness was 3.8 mm in good agreement to the UT estimated thickness of 4.2 mm.

5. Conclusions

In the study presented in this paper, a new NDE technique based on the propagation and detection of solitary waves and multivariate statistics is proposed to detect localized corrosion in steel structures. The technique consists of the use of a special transducer designed to trigger, sustain, and sense nonlinear solitary waves that interact dynamically with the structure to be monitored. The recorded waveforms are then processed with multivariate statistics based on outlier analysis to label data that diverge significantly from a set of baseline data that represent the pristine structure.

An experiment was designed to demonstrate the effectiveness of the technique. In the first experiment, three HNSW transducers were located above a thick plate subjected to localized corrosion. One of the transducers was above an area of the plate protected from the corrosion for control purposes. At the same time, a small area of the plate was probed with conventional ultrasonic pulse-echo mode testing. The results associated with the outlier analysis demonstrated that the HNSWs were able to detect corrosion as small as 0.75 mm, which in this experiment represented 12% of the plate thickness. The study was completed with two finite element models to capture the general behavior of the dynamic interaction between solitary waves and steel plates. The numerical results are in good agreement with the experimental findings, and they indicate that the time of flight and normalized amplitude of the solitary waves are strongly affected when the localized corrosion depth is higher than 50% of the plate thickness. Overall, the results show good accuracy and sensitivity of the HNSWs technique for detecting localized corrosion.

Future studies should investigate the optimal design of the array of periodic particles, i.e. material and diameter, to increase the sensitivity of the technique to the corrosion rate.

Acknowledgments

The work was supported by the U.S. National Science Foundation, Grant No. 1809932, and the American Society for Nondestructive Testing through the 2019 Fellowship Research Award granted to the first author.

ORCID iDs

Hoda Jalali https://orcid.org/0000-0002-8770-2376

Piervincenzo Rizzo https://orcid.org/0000-0002-7159-2221

References

- [1] Pipeline and Hazardous Materials Safety Administration 2019 Pipeline Significant Incident 20 Year Trend, US DOT
- [2] Wood M H, Arellano A V and Van Wijk L 2013 Corrosion related accidents in petroleum refineries. European Commission Joint Research, report no. EUR, 26331
- [3] Sharma S and Mukherjee A 2015 Ultrasonic guided waves for monitoring corrosion in submerged plates Struct. Contorl Health Monit. 22 19–35
- [4] Gallion J R and Zoughi R 2017 Millimeter-wave imaging of surface-breaking cracks in steel with severe surface corrosion *IEEE Trans. Inst. Meas.* 66 2789–91
- [5] Sedaghati A, Honarvar F and Sinclair A N 2019 Lamb wave-based experimental and numerical studies for detection and sizing of corrosion damage in metallic plates *Proc. Inst. Mech. Eng. C: J. Mech. Sci.* 233 2107–20
- Proc. Inst. Mech. Eng. C: J. Mech. Sci. 233 2107–20
 [6] Honarvar F, Salehi F, Safavi V, Mokhtari A and Sinclair A N 2013 Ultrasonic monitoring of erosion/corrosion thinning rates in industrial piping systems Ultrasonics 53 1251–8
- [7] Cheong Y-M, Kim K-M and Kim D-J 2017 High-temperature ultrasonic thickness monitoring for pipe thinning in a flow-accelerated corrosion proof test facility *Nucl. Eng. Tech.* 49 1463–71
- [8] Cawley P, Cegla F and Galvagni A 2012 Guided waves for NDT and permanently-installed monitoring *Insight-NDT Cond. Monit.* 54 594–601
- [9] Rao J, Ratassepp M, Lisevych D, Hamzah Caffoor M and Fan Z 2017 On-line corrosion monitoring of plate structures based on guided wave tomography using piezoelectric sensors Sensors 17 2882
- [10] Shen G and Li T 2007 Infrared thermography for high-temperature pressure pipe *Insight-NDT Cond. Monit.* 49 151–3
- [11] Bagavathiappan S, Lahiri B, Saravanan T, Philip J and Jayakumar T 2013 Infrared thermography for condition monitoring—A review *Infrared Phys. Technol.* 60 35–55
- [12] Cadelano G, Bortolin A, Ferrarini G, Molinas B, Giantin D, Zonta P and Biston P 2016 Corrosion detection in pipelines using infrared thermography: experiments and data processing methods J. Nondestruct. Eval. 35 49
- [13] Cheng W 2012 Pulsed eddy current testing of carbon steel pipes' wall-thinning through insulation and cladding *J. Nondestruct. Eval.* 31 215–24
- [14] Angani C, Park D, Kim G, Kim C and Cheong Y 2010 Differential pulsed eddy current sensor for the detection of wall thinning in an insulated stainless steel pipe J. Phys. D: Appl. Phys. 107 09 × 10720
- [15] Xu Z, Wu X, Li J and Kang Y 2012 Assessment of wall thinning in insulated ferromagnetic pipes using the time-to-peak of differential pulsed eddy-current testing signals NDT E 51 24–29
- [16] Safizadeh M and Hasanian M 2011 Gas pipeline corrosion mapping using pulsed eddy current technique Int. J. Adv. Manuf. Tech. 5 11
- [17] Xie S, Chen Z, Takagi T and Uchimoto T 2015 Quantitative non-destructive evaluation of wall thinning defect in double-layer pipe of nuclear power plants using pulsed ECT method NDT E 75 87–95
- [18] Schmarje N, Saillant J, Kirk K and Cochran S 2004 Imaging with lithium niobate/epoxy composites *Ultrasonics* 42 439–42
- [19] Zhang S, Eitel R E, Randall C A, Shrout T R and Alberta E F 2005 Manganese-modified Bi Sc O 3–Pb Ti O 3 piezoelectric ceramic for high-temperature shear mode sensor Appl. Phys. Lett. 86 262904
- [20] McNab A, Kirk K and Cochran A 1998 Ultrasonic transducers for high temperature applications *IEE Proc. -Sci. Meas. Technol.* 145 229–36

- [21] Megriche A, Lebrun L and Troccaz M 1999 Materials of Bi4Ti3O12 type for high temperature acoustic piezo-sensors Sensor Actuat. A-Phys. 78 88–91
- [22] Baba A, Searfass C T and Tittmann B R 2010 High temperature ultrasonic transducer up to 1000 C using lithium niobate single crystal Appl. Phys. Lett. 97 232901
- [23] Cegla F B, Cawley P, Allin J and Davies J 2011 High-temperature (> 500 C) wall thickness monitoring using dry-coupled ultrasonic waveguide transducers *IEEE Trans. Ultrason. Ferr. Freq. Cont.* 58 156–67
- [24] Dixon S, Edwards C and Palmer S 2001 High accuracy non-contact ultrasonic thickness gauging of aluminium sheet using electromagnetic acoustic transducers *Ultrasonics* 39 445–53
- [25] Kruger S, Lord M and Monchalin J P 2006 Laser ultrasonic thickness measurements of very thick walls at high temperatures AIP Conf. Proc. 820 240–7
- [26] Lee J-H and Lee S-J 2009 Application of laser-generated guided wave for evaluation of corrosion in carbon steel pipe Nat. E: Int. 42 222-7
- [27] Nesterenko V 2013 Dynamics of Heterogeneous Materials (New York: Springer)
- [28] Sen S, Hong J, Bang J, Avalos E and Doney R 2008 Solitary waves in the granular chain *Phys. Rep.* **462** 21–66
- [29] Job S, Melo F, Sokolow A and Sen S 2005 How hertzian solitary waves interact with boundaries in a 1D granular medium *Phys. Rev. Lett.* 94 178002
- [30] Coste C, Falcon E and Fauve S 1997 Solitary waves in a chain of beads under Hertz contact *Phys. Rev.* E **56** 6104
- [31] Nesterenko V F, Daraio C, Herbold E B and Jin S 2005 Anomalous wave reflection at the interface of two strongly nonlinear granular media *Phys. Rev. Lett.* 95 158702
- [32] Daraio C, Nesterenko V, Herbold E and Jin S 2005 Strongly nonlinear waves in a chain of Teflon beads *Phys. Rev.* E 72 016603
- [33] Porter M A, Daraio C, Herbold E B, Szelengowicz I and Kevrekidis P 2008 Highly nonlinear solitary waves in periodic dimer granular chains *Phys. Rev.* E 77 015601
- [34] Job S, Melo F, Sokolow A and Sen S 2007 Solitary wave trains in granular chains: experiments, theory and simulations *Granul. Matt.* 10 13–20
- [35] Carretero-González R, Khatri D, Porter M A, Kevrekidis P and Daraio C 2009 Dissipative solitary waves in granular crystals *Phys. Rev. Lett.* 102 024102
- [36] Daraio C, Nesterenko V, Herbold E and Jin S 2006 Energy trapping and shock disintegration in a composite granular medium *Phys. Rev. Lett.* 96 058002
- [37] Li F, Zhao L, Tian Z, Yu L and Yang J 2013 Visualization of solitary waves via laser Doppler vibrometry for heavy impurity identification in a granular chain *Smart Mater. Struct.* 22 035016
- [38] Yang J, Silvestro C, Khatri D, De Nardo L and Daraio C 2011 Interaction of highly nonlinear solitary waves with linear elastic media *Phys. Rev.* E 83 046606
- [39] Ni X and Rizzo P 2012 Use of highly nonlinear solitary waves in nondestructive testing *Mater. Eval.* **70** 561–9
- [40] Ni X and Rizzo P 2012 Highly nonlinear solitary waves for the inspection of adhesive joints Exp. Mech. 52 1493–501
- [41] Kim E, Restuccia F, Yang J and Daraio C 2015 Solitary wave-based delamination detection in composite plates using a combined granular crystal sensor and actuator Smart Mater. Struct. 24 125004
- [42] Yang J, Silvestro C, Sangiorgio S N, Borkowski S L, Ebramzadeh E, De Nardo L and Daraio C 2011 Nondestructive evaluation of orthopaedic implant stability in THA using highly nonlinear solitary waves *Smart Mater.* Struct. 21 012002
- [43] Yang J, Sangiorgio S N, Borkowski S L, Silvestro C, De Nardo L, Daraio C and Ebramzadeh E 2012 Site-specific

- quantification of bone quality using highly nonlinear solitary waves *J. Biomed. Eng.* **134** 101001
- [44] Yang J, Restuccia F and Daraio C 2011 Highly nonlinear granular crystal sensor and actuator for delamination detection in composite structures. *Int. Workshop on* Structural Health Monitoring
- [45] Nasrollahi A, Deng W, Rizzo P, Vuotto A and Vandenbossche J M 2017 Nondestructive testing of concrete using highly nonlinear solitary waves *Nondestruct. Test. Eval.* 32 381–99
- [46] Shelke A, Uddin A and Yang J 2014 Impact identification in sandwich structures using solitary wave-supporting granular crystal sensors Aiaa J. 52 2283–90
- [47] Rizzo P, Nasrollahi A, Deng W and Vandenbossche J 2016 Detecting the presence of high water-to-cement ratio in concrete surfaces using highly nonlinear solitary waves Appl. Sci. 6 104
- [48] Schiffer A, Alkhaja A I, Yang J, Esfahani E N and Kim T Y 2017 Interaction of highly nonlinear solitary waves with elastic solids containing a spherical void *Int. J. Solids* Struct. 118–19 204–12
- [49] Yang J, Khatri D, Anzel P and Daraio C 2012 Interaction of highly nonlinear solitary waves with thin plates *Int. J. Solids Struct.* 49 1463–71
- [50] Schiffer A and Kim T-Y 2019 Modelling of the interaction between nonlinear solitary waves and composite beams *Int. J. Mech. Sci.* 151 181–91
- [51] Singhal T, Kim E, Kim T-Y and Yang J 2017 Weak bond detection in composites using highly nonlinear solitary waves Smart Mater. Struct. 26 055011
- [52] Berhanu B, Rizzo P and Ochs M 2013 Highly nonlinear solitary waves for the assessment of dental implant mobility J. Appl. Mech. 80 011028
- [53] Nasrollahi A, Rizzo P and Orak M S 2018 Numerical and experimental study on the dynamic interaction between highly nonlinear solitary waves and pressurized balls *J. Appl. Mech.* 85 031007
- [54] Nasrollahi A, Lucht R and Rizzo P 2019 Solitary waves to assess the internal pressure and the rubber degradation of tennis balls Exp. Mech. 59 65–77
- [55] Nasrollahi A, Orak M S, James A, Weighardt L and Rizzo P 2019 A nondestructive evaluation approach to characterize tennis balls ASME J. Nondestruct. Eval. 2 011004
- [56] Nasrollahi A and Rizzo P 2018 Axial stress determination using highly nonlinear solitary waves J. Acoust. Soc. Am. 144 2201–12
- [57] Nasrollahi A and Rizzo P 2019 Numerical analysis and experimental validation of an nondestructive evaluation method to measure stress in rails ASME J. Nondestruct. Eval. 2 031002
- [58] Zener C 1941 The intrinsic inelasticity of large plates *Phys. Rev.* **59** 669–73
- [59] Sondergaard R, Chaney K and Brennen C 1990 Measurements of solid spheres bouncing off flat plates J. Appl. Mech. 112 694-9
- [60] Boettcher R, Russell A and Mueller P 2017 Energy dissipation during impacts of spheres on plates: investigation of developing elastic flexural waves *Int. J. Solids Struct*. 106-7 229–39
- [61] Jebelisinaki F, Boettcher R, van Wachem B and Mueller P 2019 Impact of dominant elastic to elastic-plastic millimeter-sized metal spheres with glass plates *Powder*. *Technol.* 356 208–21
- [62] Patil D and Higgs C F 2017 A coefficient of restitution model for sphere–plate elastoplastic impact with flexural vibrations *Nonlinear Dyn.* 88 1817–32
- [63] Müller P, Böttcher R, Russell A, Trüe M, Aman S and Tomas J 2016 Contact time at impact of spheres on large thin plates Adv. Powder Technol. 27 1233–43

- [64] Dervilis N, Cross E, Barthorpe R and Worden K 2014 Robust methods of inclusive outlier analysis for structural health monitoring J. Sound Vib. 333 5181–95
- [65] Worden K 1997 Structural fault detection using a novelty measure J. Sound Vib. 201 85–101
- [66] Worden K and Manson G 2007 The application of machine learning to structural health monitoring *Philos. Trans. R.* Soc. A 365 515–37
- [67] Worden K, Manson G and Allman D 2003 Experimental validation of a structural health monitoring methodology: part I. Novelty detection on a laboratory structure *J. Sound Vib.* 259 323–43
- [68] Worden K, Manson G and Fieller N R 2000 Damage detection using outlier analysis J. Sound Vib. 229 647–67
- [69] Rizzo P, Cammarata M, Dutta D and Sohn H 2009 An unsupervised learning algorithm for fatigue crack detection in waveguides Smart Mater. Struct. 18 025016
- [70] Zhu X P, Rizzo P, Marzani A and Bruck J 2010 Ultrasonic guided waves for nondestructive evaluation/structural health monitoring of trusses *Meas. Sci. Technol.* 21 045701
- [71] Rizzo P, Sorrivi E, Di Scalea F L and Viola E 2007 Wavelet-based outlier analysis for guided wave structural monitoring: application to multi-wire strands *J. Sound Vib.* 307 52–68
- [72] Pistone E, Li K and Rizzo P 2013 Noncontact monitoring of immersed plates by means of laser-induced ultrasounds Struct. Health Monit. 12 549–65
- [73] Mariani S, Nguyen T, Phillips R R, Kijanka P, Lanza Di Scalea F, Staszewski W J, Fateh M and Carr G 2013 Noncontact ultrasonic guided wave inspection of rails *Struct. Health Monit.* 12 539–48
- [74] Zheng B, Rizzo P and Nasrollahi A 2019 Outlier analysis of nonlinear solitary waves for health monitoring applications *Struct. Health Monit.* (http://doi.org.10.1177/ 1475921719876089)
- [75] Dubuc B, Ebrahimkhanlou A and Salamone S 2020 Stress monitoring of prestressing strands in corrosive environments using modulated higher-order guided ultrasonic waves Struct. Health Monit. 19 202–14
- [76] Schiffer A, Lee D, Kim E and Kim T-Y 2018 Interaction of highly nonlinear solitary waves with rigid polyurethane foams *Int. J. Solids Struct.* 152 39–50
- [77] Liu G-R and Quek S S 2013 The Finite Element Method: A Practical Course (Oxford: Butterworth-Heinemann)
- [78] Daraio C, Nesterenko V F, Herbold E B and Jin S 2006 Tunability of solitary wave properties in one-dimensional strongly nonlinear phononic crystals *Phys. Rev.* E 73 026610
- [79] Gunkelmann N, Serero D, Glielmo A, Montaine M, Heckel M and Pöschel T 2019 Stochastic nature of particle collisions and its impact on granular material properties *Particles in Contact-Micro* Mechanics, *Micro Process Dynamics and Particle Collective*, ed S Antonyuk (Springer International Publishing) pp 565–90
- [80] Chatterjee A 1999 Asymptotic solution for solitary waves in a chain of elastic spheres *Phys. Rev.* E 59 5912
- [81] Castagnede B, Roux J and Hosten B 1989 Correlation method for normal mode tracking in anisotropic media using an ultrasonic immersion system *Ultrasonics* 27 280–7
- [82] Ziola S M and Gorman M R 1991 Source location in thin plates using cross-correlation J. Acoust. Soc. Am. 90 2551–6
- [83] Hein I and O'brien W D 1993 Current time-domain methods for assessing tissue motion by analysis from reflected ultrasound echoes-a review *IEEE Trans. Ultrason. Ferr.* Freq. Cont. 40 84–102